

Neutron-depolarization studies on re-entrant spin glass

S. Mitsuda* and H. Yoshizawa

Institute for Solid State Physics, University of Tokyo, Roppongi, Tokyo, 106 Japan

Y. Endoh

Department of Physics, Tohoku University, Aramaki Aoba, Sendai, 980 Japan

(Received 24 October 1991)

Neutron-depolarization studies have been performed on $\text{Fe}_{0.7}\text{Al}_{0.3}$ and $\text{Au}_{0.81}\text{Fe}_{0.19}$ alloys in order to elucidate the inhomogeneous magnetic state associated with the re-entrant spin-glass (RSG) problem. The wavelength-dependent depolarization reveals that the magnetic state of the RSG, as well as the magnetic state before entering the RSG state on "mesoscopic" scale, is quite different for those alloys, in contrast to their similarity in low-field magnetization. This study illustrates that wavelength-dependent neutron depolarization provides a unique tool with which to probe the spatial magnetic state on a "mesoscopic" scale.

I. INTRODUCTION

Re-entrant spin-glass (RSG) behavior is defined by the appearance of a spin-glass state at a temperature lower than that of the long-range-ordered (LRO) state. With decreasing temperature, the RSG system first undergoes a transition from a paramagnetic state to LRO state and then changes to a spin-glass state at a certain temperature T_g . Experimentally, the RSG phase is characterized by a rapid drop of the low-field magnetization at T_g , below which an appreciable history- and time-dependent magnetization appears. Although a variety of experimental methods with different characteristic temporal and spatial windows has been used to investigate re-entrant phenomena and much experimental results have been accumulated, until recently^{1,2} the nature of the spin-glass and ferromagnetic states in a RSG seems to be not well understood.

Although there are several reasons to study RSG's by the neutron-depolarization method,^{3,4} here we only mention the significance of spatial fluctuations on a larger scale than can be examined by traditional neutron scattering by which one observes the two-spin-correlation function. Furthermore, even in small-angle neutron-scattering experiments, this spin correlation seems to behave quite differently from that measured by conventional neutron scattering.

We are interested in using the neutron-depolarization method to measure the spatial magnetic inhomogeneity on a "mesoscopic" scale. The term "mesoscopic" refers to a medium range in distance as the typical scale of ferromagnetic domains. It is known that the depolarization of the transmitted neutron beam through magnetic media occurs mostly by the inhomogeneity on this scale, and it can well be treated by integration of the processes that polarized neutrons go through in local magnetic fields. Specifically, if one observes a neutron-wavelength-dependent depolarization, one is able to speculate on the length scale of the magnetic inhomogeneity. The wavelength dependence of the depolarization of neutron

beams transmitted through a thin plate of a ferromagnet was calculated originally by Halpern and Holstein.⁵

One also easily understands that the wavelength dependence is readily obtained by using polychromatic beams of pulsed polarized neutrons. We have developed an experimental method to apply mainly to magnetic materials, and we can determine the local magnetic state on a mesoscopic scale, which is not easily done by the conventional neutron-diffraction method. Now we believe that this depolarization method provides a unique tool to look at magnetic inhomogeneity on a mesoscopic scale.^{6,7}

We chose two RSG samples, $\text{Fe}_{0.7}\text{Al}_{0.3}$ and $\text{Au}_{0.81}\text{Fe}_{0.19}$, because they are well investigated and also well recognized to be the best known ferromagnetic RSG materials. Theoretically, we have two different concepts in order to understand the RSG mechanism: the Gabay-Toulouse picture and inhomogeneous picture. The Gabay-Toulouse (GT) picture is based on a mean-field treatment of Heisenberg spins with an infinitely long-range interaction.⁸ The Mössbauer study of $\text{Au}_{0.81}\text{Fe}_{0.19}$ by Campbell *et al.*,⁹ in which the freezing of the spin component transverse to the mean magnetization was observed, is in good agreement with the GT model. The inhomogeneous picture proposed by Aeppli *et al.*¹⁰ is based on random-field effects. According to this model, the disappearance of ferromagnetic long-range order at low temperature is caused by a random molecular field due to the freezing of spins that do not participate in the ferromagnetic order. This molecular field decomposes the ferromagnetic network into finite-sized ferromagnetic clusters. Neutron-scattering experiments on RSG's such as $\text{Fe}_{3-x}\text{Al}_{1+x}$ or amorphous $\text{Fe}_x\text{Mn}_{1-x}$ have supported this picture.^{10,11} By studying the magnetic fluctuations on a mesoscopic scale by depolarization experiments, we expect to find a criterion for these models.

The format of this paper is the following: In the next section, the neutron-depolarization method using pulsed neutrons will be described in detail. Then experimental detail and analysis of the data are presented followed by the results and discussion on the RSG state. Conclusions

will be given in the final section. The magnetic-field dependence and time- or history-dependent features are planned to be presented in a separate paper.¹²

II. NEUTRON DEPOLARIZATION

We try in this section to give a detailed description of the neutron-depolarization method, in particular a proposed method using pulsed polarized neutrons and its wavelength dependence for different types of magnetic state. Neutron depolarization by ferromagnetic domains is described in previous publications.¹³ Experimental details to measure the depolarization by the sample will be discussed in the next section.

As we mentioned in the Introduction, the basic idea of the depolarization experiments is to observe the magnetic field integrated along the beam path in the magnetic medium. This observation can be made because a neutron travels with a precession described by the Larmor frequency. In this sense the method is analogous to muon-spin rotation. The essential difference between these two methods is that neutrons travel through the sample while muons are trapped at certain sites in the sample. Therefore the local magnetic field detected by neutron spins is integrated. All the local information is automatically averaged out, but the data still contain useful information, as we shall describe below.

Let us consider the polarized-neutron passage in a magnetic medium where the beam cross section is pretty narrow, as shown in Fig. 1. We call it a subbeam, within which the internal magnetic field $\mathbf{B}(r)$ can be defined along the neutron path. For the sake of simplicity, all of the incident neutron-polarization vectors \mathbf{P}_i are polarized along the z direction in Fig. 1; i.e., $|\mathbf{P}_i|=1$. Immediately after the neutrons enter the magnetic medium, the polarization vector \mathbf{P} starts to precess around the local field $\mathbf{B}(r)$. The motion of \mathbf{P} just follows the simple classical equation of motion,

$$\frac{d\mathbf{P}}{dt} = \gamma \mathbf{P} \times \mathbf{B}(r=vt), \quad (1)$$

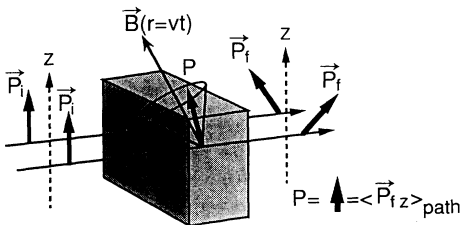


FIG. 1. Schematic drawing of the Larmor precession of a neutron-polarization vector \mathbf{P} of a subbeam in a magnetic material: \mathbf{P}_i is the incident polarization vector which is fully polarized along the z direction. \mathbf{P}_f is the final polarization vector of a subbeam which points out in some direction, reflecting the Larmor precession around the internal field $\mathbf{B}(r)$ along the neutron subbeam. P is the polarization of the whole transmitted beam used in the experiment, which is defined by the average of the z component of the vector \mathbf{P}_f over all subbeams. Note that the norm of the polarization vector of the subbeams is kept to unity, namely, $|\mathbf{P}_i|=|\mathbf{P}|=|\mathbf{P}_f|=1$.

where γ is the neutron gyromagnetic ratio and r is the coordinate along the flight path, which is related to the neutron velocity v by $v=r/t$. The validity of the application of the classical equation of motion in the neutron-polarization determination is already confirmed both theoretically and empirically.¹⁴ The final polarization vector \mathbf{P}_f is determined just at the end point of the magnetic medium. As mentioned previously, \mathbf{P}_f is dependent on the neutron velocity or wavelength because of the different traveling time in the medium. The polarization P of the whole transmitted beam, which is obtained experimentally, is defined by the average of the z component of the vector \mathbf{P}_f over all subbeams. In order to derive the formula for the wavelength-dependent polarization $P(\lambda)$ necessary for the depolarization experiments, we categorize the mesoscopic inhomogeneity into four types, as illustrated in Fig. 2(a)–2(d).

(a) Paramagnetic and pure spin-glass state: Magnetic inhomogeneity on an atomic scale (spin-glass state) and fast fluctuations of the local field in the media (paramagnetic state) have no effect on the neutron polarization, as depicted in Fig. 2(a). Clearly, neutrons do not depolarize in a medium in the paramagnetic state because the temporal spin fluctuation is too fast (10^{-12} sec or shorter) for the neutron polarization to follow the variation of the magnetic field $B(t=r/v)$ acting on the moving neutron. This situation is similar to the motional narrowing phenomenon in spin-resonance experiments. In the spin-glass phase, a similar fast variation of the magnetic field results not from temporal spin fluctuation, but from spatial spin fluctuation, because each spin is in a frozen state

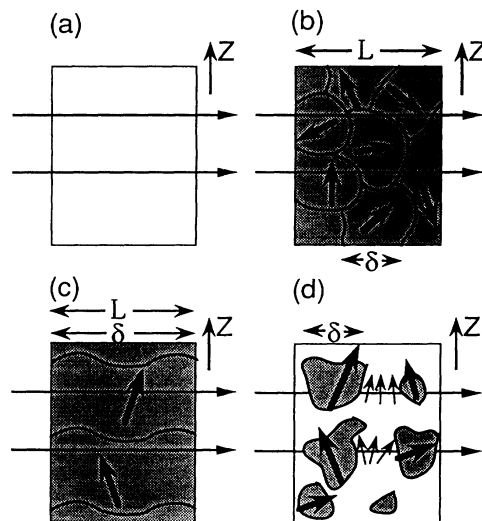


FIG. 2. Schematic drawing of typical magnetic inhomogeneities: (a) spin-glass case, (b) ferromagnetic multidomain case, (c) ferromagnetic monodomain case, and (d) superparamagnetic-like case. The sample is magnetized along the z axis. White and hatched regions correspond to pure spin-glass and ferromagnetically aligned regions, respectively. The arrow represents the direction of the local magnetization of each domain or cluster. The small arrows in the white region of model case (d) represent the stray field from the clusters.

and points in a random direction on a microscopic scale. When the neutrons travel through the sample, they feel an effective fast variational field $B(t)$ generated by the spin-glass configuration. In fact, no depolarization is confirmed in the pure spin-glass state of two well-known spin-glass materials: amorphous Fe-Mn (Ref. 15) and Au-Fe.¹⁶ Here “pure spin glass” means that the sample exhibits only the spin-glass phase; in other words, the sample does not show a re-entrant spin-glass transition.

(b) Ferromagnetic multidomain state: In this case the linear dimension of a ferromagnetic domain is small compared with the sample thickness, as depicted in Fig. 2(b), so that each neutron sees a series of many domains. This situation is widely realized in the demagnetized state of usual ferromagnetic substances in low magnetic fields. A classical treatment of neutron depolarization by multiferromagnetic domains originally was given by Halpern and Holstein.⁵ They gave the wavelength dependence of depolarization for two limiting cases (the Larmor phase in a domain is very smaller or larger than 2π). In their calculation, (1) uniform magnetic induction within a domain, (2) domain walls of negligible thickness, (3) no correlation between the magnetic orientation of a domain and its size, and (4) no correlation between the orientations of successive domains are assumed. Extending their treatment to general wavelength regions, Mitsuda and Endoh¹³ derived the wavelength-dependent polarization $P(\lambda)$ for type (b):

$$P(\lambda) = \left\langle \left\langle \frac{B_{\parallel}^2}{B^2} \right\rangle_{\mathbf{B}} + \left\langle \frac{B_{\perp}^2}{B^2} \right\rangle_{\mathbf{B}} \langle \cos(cB\delta\lambda) \rangle_{\delta} \right\rangle^N, \quad (2)$$

where the brackets $\langle \cdots \rangle_{\mathbf{B}}$ and $\langle \cdots \rangle_{\delta}$ represent the ensemble average over the local induction in each domain and the domain size, respectively. The symbols \parallel and \perp indicate the components of the local induction \mathbf{B} parallel and perpendicular to the bulk magnetization of the sample. N is the average number of the domains that neutrons pass through and is equal to L/δ , where L is the sample thickness and δ is the average domain size. The constant c in the argument of the cosine is related to the Larmor phase $cB\delta\lambda$ of the precession of neutron polarization within a domain and is expressed by $\gamma m/h$, with standard physical constants.¹⁷ Although the second term introduces an oscillation of the polarization with respect to the neutron wavelength, it is averaged out by the wide distribution of domain sizes, as well as the multiplication operation by the large number of N . Depending on the characteristic Larmor phase $cB\delta\lambda$ in one domain with size δ , $P(\lambda)$ then exhibits asymptotic behavior such as either the $\exp(-\alpha\lambda^2)$ law⁵ in the case ($cB\delta\lambda \ll 2\pi$), the $\sim \exp(-\beta\lambda)$ law¹³ in the case ($cB\delta\lambda \sim \pi/2$), or the λ -independent law⁵ in the case ($cB\delta\lambda > 2\pi$) within the wavelength range measured in the experiment. Here the coefficient α has been given by

$$\alpha = \frac{1}{2} \left\langle \frac{B_{\perp}^2}{B^2} \right\rangle_{\mathbf{B}} c^2 B^2 \delta \lambda. \quad (3)$$

The coefficient α is determined by the degree of domain orientation, strength of induction B , and average domain

size δ .

(c) Ferromagnetic monodomain state: This case is similar to the previous one, but this time each domain extends over the entire sample along the beam direction, as depicted in Fig. 2(c); thus each neutron sees only one domain. Namely, this case corresponds to case (b) with $N=1$ and $\delta=L$. These large domains can be expected for a ferromagnetic sample with a thin plate shape. For such a domain configuration, the effect of the second term in Eq. (2) becomes measurable. In other words, the neutron-polarization vector of each subbeam continuously makes precessions with the same Larmor phase $cBL\lambda$ throughout the sample. Then the observed $P(\lambda)$ shows an oscillation with respect to the neutron wavelength,

$$P(\lambda) = P_0 + (1 - P_0) \cos(I\lambda), \quad (4)$$

where P_0 is given by

$$P_0 = \left\langle \frac{B_{\parallel}^2}{B^2} \right\rangle_{\mathbf{B}}, \quad (5)$$

representing how the ferromagnetic domains or cluster align along the applied external field. I is the field integral and is expressed as

$$I = cBL. \quad (6)$$

Experimentally, however, nonuniformity in the sample thickness L or finite divergence of the beam can produce the damping of oscillations even for this case, since the effective total path length has a distribution. If we express the distribution of the effective total path length L by the Gaussian distribution with a half width of ΔL , the profile $P(\lambda)$ can be expressed by

$$P(\lambda) = P_0 + (1 - P_0) e^{-\sigma_I \lambda^2} \cos(I\lambda), \quad (7)$$

where the damping rate σ_I has a simple relation to I , given by

$$\frac{\sqrt{2\sigma_I}}{I} = \frac{\Delta L}{L} = \text{const.} \quad (8)$$

Therefore it can be readily distinguished from the intrinsic mesoscopic inhomogeneity expected in a “superparamagneticlike state” which will be discussed next, by wavelength-dependent depolarization experiments.

It should be pointed out that the damped oscillatory feature is also observed in the situation of a “incomplete monodomain state” just before the state changes from a “multidomain state” to a “complete monodomain state” in the magnetization process, similarly because of the distribution of the effective total path length.

(d) Superparamagneticlike state: Finally, we consider the most interesting case in which ferromagnetic “clusters” are floated in a pure spin-glass medium, as depicted in Fig. 2(d). For the sake of convenience for later discussions, we call this case *superparamagneticlike*. Here we used the term “cluster” instead of the term “domain.” This superparamagneticlike state is apparently similar to the ferromagnetic multidomain state [case (b)] in the sense that a uniform internal field is realized within a cluster or a domain. However, there is an essential

difference between cases (d) and (b). While the ferromagnetic domain wall separates the internal magnetic field rigidly in the ferromagnetic multidomain case, there exists no sharp boundary dividing the internal magnetic field in the superparamagneticlike case. In the case of ferromagnetic multidomains (b), the polarization $P(\lambda)$ is given by the N th power of the depolarization in each constituent domain, as shown in Eq. (2). It results from the segmentation of the Larmor precession due to the *non-adiabatic* change of the direction of the local magnetization from domain to domain.³ On the other hand, in this superparamagneticlike case, because of a stray field from the clusters, the internal magnetic field may be *adiabatically* connected throughout the sample, as schematically shown in Fig. 2(d). Thus the neutron-polarization vector may make precessions continuously from one cluster to the next, or the polarization follows adiabatically throughout the sample. Taking account of the results on the pure spin-glass state discussed above [case (a)], we assume that the Larmor precession essentially takes place within a ferromagnetic cluster, since no net magnetic field exists in the spin-glass region itself except a stray field from the clusters, as indicated by white area in Fig. 2(d). Under these assumptions we obtain the same formula as in Eq. (4), but Eq. (6) must be modified as follows:

$$I = cB \langle (\delta_1 + \delta_2 + \dots) \rangle_{\text{path}}. \quad (9)$$

Here, as for the orientation of clusters, it is assumed that the orientations of each cluster on the neutron-beam path are similar to each other to satisfy the addition of the Larmor phase in Eq. (9). Equation (9) expresses that the field integral I is determined not by the sample thickness L , but by the sum of the length of each cluster the neutrons pass through. Note that, when the magnetic induction B is known, we can estimate the effective volume fraction of the ferromagneticlike clusters in the sample from I :

$$\begin{aligned} \text{effective volume fraction} &= \frac{\langle (\delta_1 + \delta_2 + \dots) \rangle_{\text{path}}}{L} \\ &= \frac{I}{cBL}. \end{aligned} \quad (10)$$

Since the experiments are carried out with a finite cross section of the neutron beam, the field integral value of each neutron passage has a distribution, and an appropriate average over the beam area must be taken as denoted by $\langle \dots \rangle_{\text{path}}$. We can express such an average by the Gaussian distribution centered at the average value of I with a half width of $\sqrt{2\sigma_I}$ and then obtain the same expression for $P(\lambda)$ as Eq. (7), namely, $P(\lambda) = P_0 + (1 - P_0)e^{-\sigma_I \lambda^2} \cos(I\lambda)$.

Here the damping factor $\exp(-\sigma_I \lambda^2)$ represents the fact that the distribution of I over the beam size causes a decay of the oscillation in $P(\lambda)$. In our definition the full width of the distribution of I is given by $2\sqrt{2\sigma_I}$. Thus the damping factor determined by the data analysis contains the information on the degree of the *mesoscopic* inhomogeneity. Suppose the system is inhomogeneous on a

microscopic scale; then the field integral value I has an extremely narrow distribution function. Clearly, the depolarization technique does not detect such a *microscopic* fluctuation. In other words, such an inhomogeneous magnetic field on a microscopic scale is coarse grained as an averaged homogeneous one on a mesoscopic scale, which is the appropriate scale for the depolarization technique. Namely, in this limit, the situation of a superparamagneticlike state becomes equivalent to the situation of ferromagnetic monodomain state. We believe that if damping of the oscillation is observed, except the trivial effect described before, it is evidence that the system does not have microscopic but has mesoscopic inhomogeneities. It is, however, not possible to obtain quantitative information on the size or the shape of clusters, because σ_I comes not from the distribution of each cluster size, but the distribution of the sum of the cluster size.

In this study of spin-glass materials, we concentrate on the several mesoscopic inhomogeneities expected in the pure spin-glass phase (a), in the superparamagneticlike phase (d), or even in the ferromagnetic phases (b) or (c), which essentially determine the bulk properties of the materials. Although the real situation might not be quite as simple as we presented in this section, we attempt to interpret our data guided by these four typical situations.

III. EXPERIMENTAL DETAILS AND DATA ANALYSIS

A. Sample preparation

Polycrystalline ingots of both $\text{Fe}_{0.7}\text{Al}_{0.3}$ and $\text{Au}_{0.81}\text{Fe}_{0.19}$ were prepared at Tohoku University by quenching from the molten state in an induction furnace to a cell at ambient temperature attached to a furnace under Ar atmosphere. The samples for neutron-depolarization experiments were shaped to a disk plate. Because we must determine the optimum thickness empirically after preliminary measurement, the samples were cut at a thickness of about 0.4 mm. Further annealing treatment was done only for the $\text{Au}_{0.81}\text{Fe}_{0.19}$ sample after cutting, because we were concerned that the cold work as well as thermal relaxation might change the bulk properties considerably. Therefore it was homogenized at 900°C for approximately 50 h and was kept in liquid nitrogen after quenching.

The bulk magnetization was measured with a vibrating-sample magnetometer at Tohoku University. The temperature dependence of the low-field magnetization in zero-field-cooled (ZFC) and field-cooled (FC) scans for $\text{Au}_{0.81}\text{Fe}_{0.19}$ and $\text{Fe}_{0.7}\text{Al}_{0.3}$ samples are presented in Figs. 3(a) and 3(b). Our data are consistent with the previous results presented by Shull, Okamoto, and Beck¹⁸ for $\text{Fe}_{0.7}\text{Al}_{0.3}$ and by Coles, Sarkissian, and Taylor¹⁹ for $\text{Au}_{0.81}\text{Fe}_{0.19}$ polycrystalline samples. Transition temperatures are determined to be $T_c \sim 470$ K, $T_c^{\text{inv}} \sim 177$ K, and $T_g \sim 77$ K for the Fe-Al sample and $T_c \sim 175$ K and $T_g \sim 25$ K for the Au-Fe sample. Here T_c , T_g , and T_c^{inv} are the Curie, RSG, and inverse Curie temperatures, respectively. Note that the $\text{Fe}_{0.7}\text{Al}_{0.3}$ system has a magnetic state like the superparamagnetic state between ferromagnetic and RSG phases. T_g and T_c^{inv} are defined as

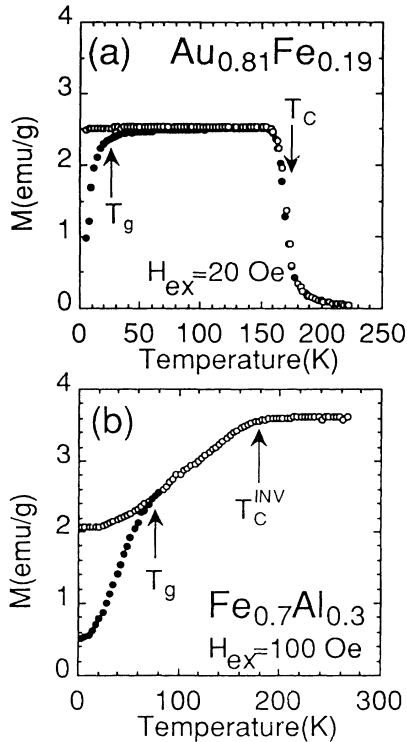


FIG. 3. Temperature dependence of the low-field magnetization (a) of $\text{Au}_{0.8}\text{Fe}_{0.19}$ at an external magnetic field $H_{\text{ex}} = 20$ Oe and (b) of $\text{Fe}_{0.7}\text{Al}_{0.3}$ at $H_{\text{ex}} = 100$ Oe. The solid and open symbols correspond to zero-field-cooled ZFC and field-cooled (FC) scans, respectively.

the temperatures below which strong irreversibility in the magnetization sets in and the magnetization deviates from the demagnetization controlled plateau, respectively.

B. Neutron-depolarization measurements

Neutron-depolarization measurements were performed on the TOP spectrometer installed at the cold-neutron guide hall of the Booster Synchrotron Utilization Facility

at KEK (National Laboratory for High Energy Physics) in Tsukuba. Although a full description of the TOP spectrometer has been given elsewhere,^{20,21} here we describe some necessary experimental details for the depolarization measurements. A schematic drawing for the experimental setup to measure depolarization is shown in Fig. 4. Pulsed neutron beams with wavelength range approximately from 3 to 9 Å were polarized by total-reflection-type magnetic mirrors which were assembled as curved Soller slits.²¹ Then the polarization of the incident neutrons was flipped by switching the polarity of the electric current in the front coaxial coil of a Drabkin-type spin flipper²¹ so that the direction of the polarization vector in front of the sample was parallel or antiparallel to the external magnetic field applied to the sample. After the sample the polarization of the transmitted beam was analyzed by similar curved Soller-type magnetic mirrors. Time-of-flight spectra of neutron intensities $I_{\text{on}}(\lambda)$ and $I_{\text{off}}(\lambda)$ were accumulated corresponding to spin flipper status “on” or “off.” The polarization $P(\lambda)$ of the transmitted beam through the sample defined in Sec. II is then obtained by

$$P(\lambda) = \frac{[I(\lambda)]_{\text{off}} - [I(\lambda)]_{\text{on}}}{[I(\lambda)]_{\text{off}} + [I(\lambda)]_{\text{on}}} \frac{1}{P_i^2(\lambda)}. \quad (11)$$

The incident beam polarization $P_i(\lambda)$ was measured with the sample removed, keeping exactly the same configuration for the scan with the sample in order to calibrate the incomplete polarizing efficiency of polarizer and analyzer. Since our spin flipper has an excellent flipping efficiency for all wavelengths measured,²¹ calibration associated with the spin flipper was neglected.

The sample was mounted at the cold end of a closed-cycle variable-temperature cryostat (10–300 K). The neutron-beam cross section was restricted to about a 6-mm diameter by a cadmium beam narrower. An external field was applied up to 150 Oe along the vertical direction, which is parallel to the sample plate, by Helmholtz coils. To avoid beam depolarization at the zero-field point of Helmholtz coils on the neutron-beam path, permanent guide magnets were put in the front of as well as behind the Helmholtz coils.

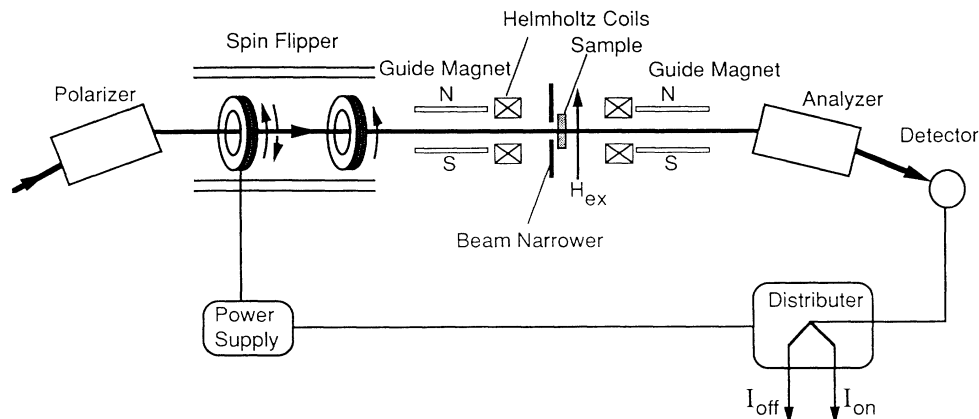


FIG. 4. Schematic drawing of experimental setup to measure neutron depolarization.

The wavelength dependence of the polarization in the two RSG alloys has been measured in a wide range of temperatures, covering the paramagnetic, ferromagnetic, and RSG phases. The measurements were performed in both ZFC and FC scans. The ZFC scan corresponds to the way in which the sample is cooled down in zero external magnetic field through T_g from room temperature, and the depolarization is measured upon heating step by step in a small field. The applied external field H_{ex} was 100 and 31 Oe for the Fe-Al and Au-Fe samples, respectively. For the FC scan the measurements were performed on cooling stepwise under the same external field H_{ex} as in the ZFC scan. One thermal scan requires more than 24 h even though each point is measured in about less than 1 h. Typical depolarization profiles $P(\lambda)$ at designated temperatures of each phase are shown for both ZFC (denoted by solid circles) and FC (denoted by open circles) scans in Fig. 5.

The profile $P(\lambda)$ in Fig. 5(e) shows that no depolarization occurs in the paramagnetic phase of the Au-Fe sample, being consistent with the model in Fig. 2(a). In the ferromagnetic phase above T_g , the profile in Figs. 5(b)

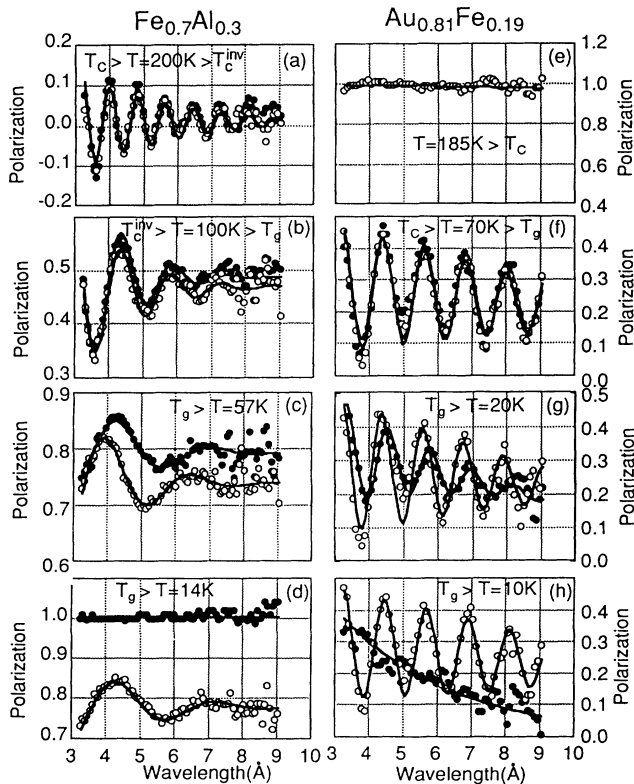


FIG. 5. Typical wavelength dependence of the polarization $P(\lambda)$ for both systems $\text{Fe}_{0.7}\text{Al}_{0.3}$ and $\text{Au}_{0.81}\text{Fe}_{0.19}$. To the left: $P(\lambda)$ for $\text{Fe}_{0.7}\text{Al}_{0.3}$ in the (a) ferromagnetic, (b) superparamagneticlike, and (c) and (d) RSG phases. To the right: $P(\lambda)$ for $\text{Au}_{0.8}\text{Fe}_{0.19}$ in the (e) paramagnetic (f) ferromagnetic, and (g) and (h) RSG phases. Solid and open symbols correspond to ZFC and FC scans, respectively. The solid line is the result of a fitting procedure. T_c , T_g , and T_c^{inv} are the Curie, RSG, an inverse Curie temperatures, respectively.

and 5(f) is characterized by damped oscillations for both samples, which tell us that the ferromagnetic-monodomain state or superparamagneticlike state, as described in the models in Figs. 2(c) and 2(d). Which magnetic state is realized in each system will be clear later by checking the thermal evolution of the damping rate σ_I . No appreciable field-cooling effect was observed, as the two profiles for ZFC and FC scans in Figs. 5(a), 5(b), and 5(f) fall together. In contrast, pronounced differences in the profile $P(\lambda)$ for ZFC and FC scans below T_g are visible, as seen in Figs. 5(c), 5(d), 5(g), and 5(h), being consistent with the hysteresis observed in the magnetization data shown in Fig. 3.

As for the FC scan, the damped oscillatory feature seen above T_g for both samples still remains down to the lowest temperature, although the periodicity of oscillation as well as the damping rate are different from those in the ferromagnetic phase. However, ZFC profiles below T_g show entirely different behavior for the two samples. For the Fe-Al sample, the ZFC profile $P(\lambda)$ exhibits no depolarization at the lowest temperature, $P(\lambda)=1$, as seen in Fig. 5(d), which indicates that the ZFC state at this temperature in the RSG phase of the Fe-Al sample is close to a pure spin-glass state in which the coarse-grained internal magnetic field on mesoscopic scale is essentially zero, as described in the model in Fig. 2(a). With increasing temperature, gradually a damped oscillatory feature with a damping rate similar to the FC scan appears, as seen in Fig. 5(c). On the other hand, the ZFC profile for the Au-Fe sample shows an exponential damping without oscillation at the lowest temperature, $P(\lambda)=\exp(-\beta\lambda)$, as seen in Fig. 5(h), which suggests that the ZFC state at this temperature in the RSG phase of the Au-Fe sample is close to a demagnetized state consisting of many small ferromagnetic domains, as described in the model in Fig. 2(b), in which essentially ferromagnetic long-range order remains, as predicted by the GT model. With increasing temperature, a damped oscillatory feature with larger damping rate compared with the FC scan appears and recovers up to T_g , as seen in Fig. 5(g).

This qualitative difference of ZFC profiles $P(\lambda)$ between two samples may suggest that the RSG states of Fe-Al and Au-Fe samples are quite different, although the low-field magnetization of both systems shows the similar rapid drop at low temperature. This point will be discussed quantitatively later.

C. Analysis and discussions

We parametrized the wavelength-dependent polarization $P(\lambda)$ by fitting the measurements (except several ZFC profiles at low temperature) to

$$P(\lambda) = P_0 + A e^{-\sigma_I \lambda^2} \cos(I\lambda + s). \quad (12)$$

In this equation we extended Eq. (7) by adding a *phase shift* s in the argument of the cosine factor and by putting the coefficient A instead of $(1 - P_0)$. Those are necessary to account for the deviation of the direction of the magnetic guide field at the surface of the sample from the z axis due to the stray field from the sample itself. Since

the sum rule $A + P_0 = 1$ is not satisfied in such situation, we treat the coefficient A as a free parameter. Note that the damping rate of the oscillation, σ_I , and the field integral I are free from this effect. The results of this fitting procedure for the parameters P_0 , σ_I , and I are summarized in Fig. 6. For comparison, we reproduced the temperature dependence of the low-field magnetization in Figs. 6(a) and 6(e).

In order to understand the thermal evolution of the field integral I shown in Figs. 6(d) and 6(h), one should recall Eq. (6) or (9), which relates the field integral I to the local induction B as well as to the effective path length. For example, the field integral I of a normal ferromagnet should increase monotonically with decreasing temperature below T_c and saturate at low temperatures, reflecting the usual thermal evolution of local induction B . However, in both samples studied here, an anomalous decrease of the field integral I is observed at low temperature. For the Au-Fe sample, it initially increases below T_c as the temperature is lowered, reaches a maximum at approximately 50 K, and then shows a small decrease as well as hysteresis below T_g . For the Fe-Al sample, it shows a dramatic decrease on lowering the temperature after it shows a maximum around room temperature. It should be noted that we confirmed that the field integral I for the Fe-Al sample increases below $T_c \sim 470$ K, as for a usual ferromagnet, consistent with the behavior of the Au-Fe sample near T_c . In both cases, the decrease of the

field integral I observed in the RSG phase of both the Au-Fe and Fe-Al samples should be interpreted as an indication that sample enters into a RSG phase from the ferromagnetic phase. The decrement of the field integral I at low temperature is different in the two samples, simply because it depends on the distance of each of the samples from the multicritical point in the RSG phase diagram where the paramagnetic, ferromagnetic and spin-glass phases meet. This is a topic that we discussed in a separate paper²² along with the data of a Au-Fe sample of different composition.

Although, qualitatively, a similar anomaly of the field integral I is seen in both samples, the thermal evolution of the damping rate σ_I has entirely different characteristics, as seen in Figs. 6(c) and 6(g). For the Au-Fe sample, σ_I is weakly temperature dependent in the ferromagnetic phase and shows a rapid increase below T_g only for the ZFC scan. On the other hand, for the Fe-Al sample, the damping rate σ_I in both FC and ZFC scans increases below T_c^{inv} and reaches a maximum around 100 K just before entering the RSG phase. For the Au-Fe sample, the weakly temperature-dependent σ_I presumably results from a trivial effect, i.e., the distribution of the effective path length, which was discussed in the last section. An estimated distribution of the effective path length $\Delta L/L$ using Eq. (8) is about 3%. This amount of distribution can be attributed to the nonuniformity of the sample thickness due to our cold-work procedure in sample preparation.

In the case of the Fe-Al sample, however, such an effect cannot explain the thermal evolution of σ_I . In order to interpret the experimental results of the Fe-Al sample, in particular, the thermal evolutions of σ_I and I , we have drawn the magnetic states in the Fe-Al sample schematically in Fig. 7. As the Fe-Al sample is cooled in the ferromagnetic phase below room temperature, small spin-glass-like regions start to appear inside the large ferromagnetic domain state, as shown in Fig. 7(a). Upon further cooling the spin-glass-like regions become larger in size, which causes a decrease of the effective volume fraction that is in the ferromagnetic state. Here the effective volume fraction means the total length along the path of the neutrons with the magnetic induction B , as discussed for the explanation of Eq. (10). Schematically, it corresponds to the averaged total length of the hatched area in Fig. 7. Below T_c^{inv} , where the bulk magnetization starts to decrease substantially, the mesoscopic state may vary from Fig. 7(a) to 7(b). An important difference between them is that spontaneous bulk magnetization is not expected for the state in Fig. 7(b) because of the lack of connectedness of the ferromagnetic region, as is present in Fig. 7(a). Here we would like to note that the assumption made for case (d) in Sec. II for cluster orientation might be satisfied. Namely, since the magnetic state is a ferromagnetic monodomain state above T_c^{inv} , the direction of each cluster on the neutron-beam path can be similar to each other even after decomposition to a finite cluster below T_c^{inv} . Then, upon further cooling in zero external field, the size of the ferromagnetic clusters becomes smaller and smaller. Therefore, as the mesoscopic state changes from Fig. 7(a) to 7(c), the field integral I de-

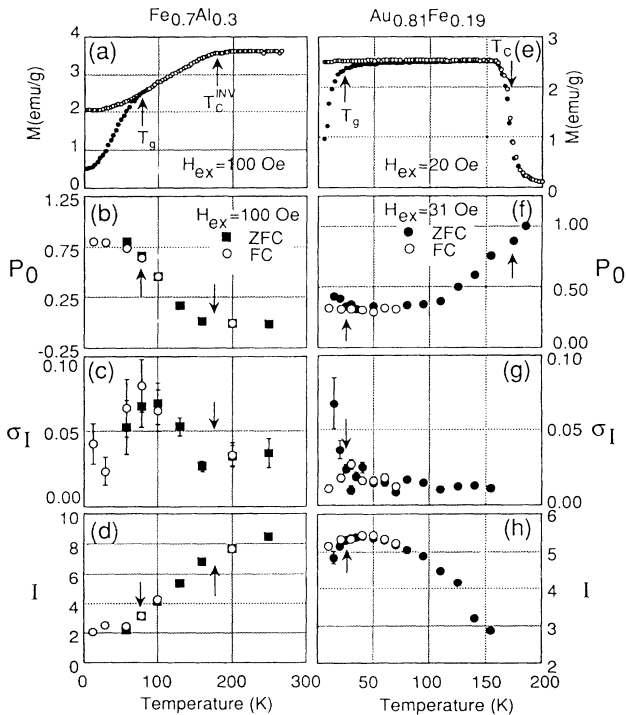


FIG. 6. Temperature dependence of the low-field magnetization and fitted parameters P_0 , σ_I , and I from neutron depolarization for both systems $\text{Fe}_{0.7}\text{Al}_{0.3}$ (left side) and $\text{Au}_{0.81}\text{Fe}_{0.19}$ (right side). The solid and open symbols correspond to ZFC and FC scans, respectively. External magnetic fields $H_{\text{ex}} = 100$, 20, and 31 Oe were used for (a)–(d), (e), and (f)–(h), respectively.

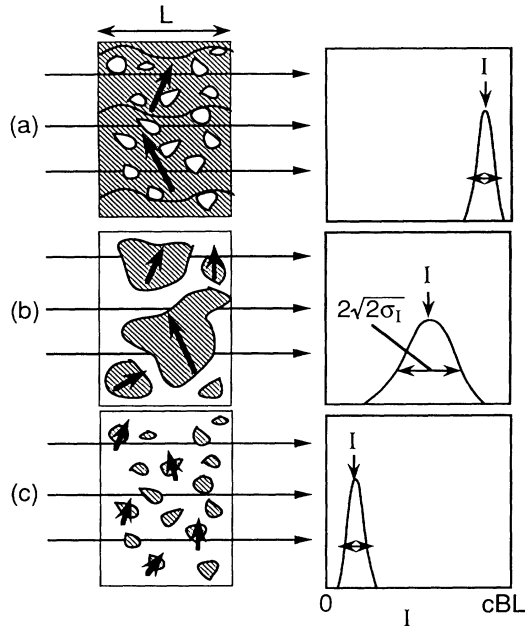


FIG. 7. Schematic drawings of the neutron passage through the sample which is at a typical stage of decomposition of a ferromagnetic network and corresponding distribution functions of the field integral over the beam size. White and hatched regions correspond to pure spin-glass and ferromagnetically aligned regions, respectively. The arrow represents the direction of the local magnetization of each cluster.

creases, reflecting the decrease of the effective volume fraction of the ferromagnetic region. This explains why I decreases as the Fe-Al sample enters into the RSG phase.

Now we turn to the schematic temperature dependence of σ_I . In Fig. 7 the damping rate σ_I is represented by the width of the distribution function of I . Note that we defined σ_I by the full width at half maximum of the Gaussian distribution of I , which is equal to $2\sqrt{2}\sigma_I$, as was introduced in Eq. (7). We expect that σ_I changes in such a way that it reaches the maximum where the fraction of the ferromagnetic region reaches nearly half of the sample volume; in other words, σ_I shows a maximum when it becomes comparable with that of the spin-glass region. Indeed, the experimental result for the Fe-Al sample is consistent with this picture, as seen in Fig. 6(c). Note that the field integral I at $T \sim 100$ K, where σ_I shows its maximum, is nearly half of the value of I at room temperature where the volume fraction of the ferromagnetic region could be almost unity. Here we assume that the thermal evolution of the magnetic induction B itself is almost saturated below room temperature because T_c is about 470 K and is well above room temperature. It should be noted that the width of the distribution of field integral depends on a mutual relation sample thickness and cluster size. One can expect the intrinsic width of the field integral distribution only for the case that the sum of cluster sizes along each path of subbeams has finite distribution. Namely, it means that the characteristic scale of cluster sizes is not very small compared with sample thickness L in this Fe-Al sample case.

The finite value of σ_I observed around room temperature should be attributed to the nonuniformity of the sample thickness, as in the case of Au-Fe.

In addition to the interesting temperature dependence of σ_I which supports a mesoscopic inhomogeneous picture for Fe-Al, we present a plot of σ_I as a function of field integral I for various temperatures and magnetic fields, as seen in Fig. 8(b). As shown in Fig. 8(a), I is almost magnetic-field independent in the ferromagnetic phase, while it becomes magnetic-field dependent in the superparamagneticlike phase. Thus, by changing the magnetic field, we can obtain the magnetic state with various field integrals I , in other words, with a different volume fraction of the ferromagnetic region. If our mesoscopic inhomogeneous picture is correct, we must see that the plot of σ_I vs I for various temperatures and magnetic fields shows its maximum. Indeed, as seen in Fig. 8(b), the damping rate σ_I shows its maximum at $I \sim 4$, which is nearly half of the value of I at room temperature where the volume fraction of the ferromagnetic region could be almost unity. We believe it is an indication that the Fe-Al sample has mesoscopic magnetic inhomogeneities. It should be noted that for the Au-Fe sample such interesting behavior of σ_I was not observed experimentally.

As was explained above, the difference in behavior of σ_I between the Au-Fe and Fe-Al samples is significant evidence to indicate that the coarse-grained magnetic

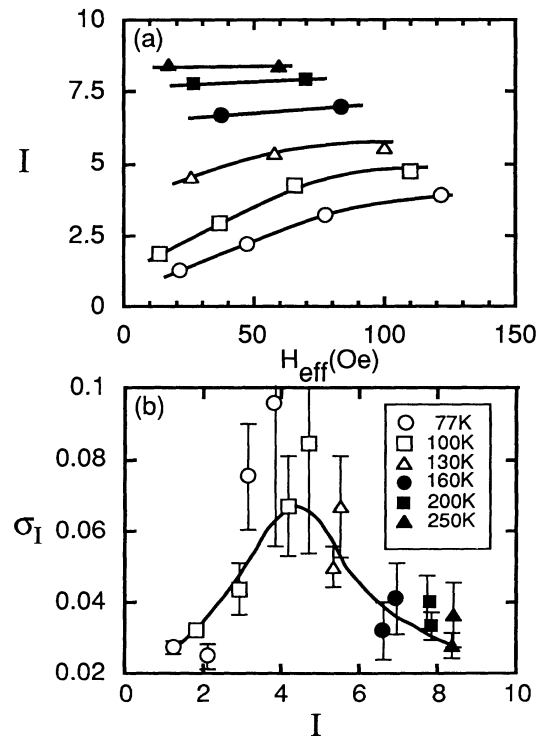


FIG. 8. (a) Magnetic-field dependence of the field integral I for various temperatures. Here H_{eff} is effective magnetic field where the demagnetizing field is corrected. (b) Plot of the damping rate σ_I vs the field integral I for several temperatures and magnetic fields.

states entering the RSG phase on a mesoscopic scale are quite different in the Au-Fe and Fe-Al samples. Now we return to the ZFC magnetic states in the RSG phase in the Au-Fe and Fe-Al samples. In the last section, we explained that the ZFC magnetic state of the Au-Fe sample in the RSG phase is close to a demagnetized state consisting of many small ferromagnetic domains, as found in a normal ferromagnet. We can roughly estimate the average size δ of the ferromagnetic domains realized at the lowest temperature in the ZFC scan, using the criterion that the polarization exhibit exponential behavior of the type $P(\lambda) = \exp(-\beta\lambda)$ when the characteristic Larmor phase in one domain is around $\pi/2$,¹³ namely,

$$cB\delta\lambda \sim \pi/2. \quad (13)$$

Using the field integral value in the FC case, $I = cBL \sim 5$, as seen in Fig. 6(h), the average domain size δ can be estimated to be $\sim 25 \mu\text{m}$, which seems reasonable as a typical ferromagnetic domain size. Here it is assumed that the local magnetization density B itself is same for both ZFC and FC scans and that a lower value of the low-field magnetization in the ZFC scan than in the FC scan comes from the difference of domain structure, as we presented in the last section. It should be pointed out that the existence of ferromagnetic domains in the RSG phase for $\text{Ni}_{1-x}\text{Mn}_x$ and amorphous Fe-Mn is demonstrated by recent electron microscopy experiments,²² as well as by recent depolarization experiments.^{15,23}

As the temperature is raised in the ZFC scan, $P(\lambda)$ recovers the oscillation, as shown in Figs. 5(h) and 5(g). This is evidence for the fact that frozen or blocked small domains at the lowest temperature in the RSG phase gradually grow into monodomains up to $T_g \sim 25 \text{ K}$ as a result of thermal activation. The rather large damping rate σ_I as well as the slightly lower value of the field integral I in the ZFC scan just below T_g seen in Figs. 6(g) and 6(h) can be attributed to the incomplete monodomain state just before the state changes from a multidomain state to a complete monodomain state up to T_g .

Let us return now to the ZFC magnetic state in the RSG phase of the Fe-Al sample. In the last section, we explained that the ZFC state at the lowest temperature in the RSG phase of the Fe-Al sample is close to a pure spin-glass state where the coarse-grained internal magnetic field on the mesoscopic scale is essentially zero, because the profile $P(\lambda)$ exhibits no depolarization within experimental accuracy. It means that the characteristic scale of the spatial fluctuation of the local magnetization is not mesoscopic but microscopic. Although in this situation the ferromagnetic domain formula of Eq. (3) is not applicable, we may show how the small domain size δ is required to give no depolarization within experimental accuracy. For example, an average domain size δ of less than 100 \AA is required so that polarization at a wavelength of 8 \AA has more than 0.99. Here the following two numbers are used. First is the magnetic induction B determined from the field integral $I = cBL \sim 8$ around room temperature, which is assumed to be almost saturated at low temperature. And second is a domain orientation factor $\langle B_{\perp}^2/B^2 \rangle = \frac{2}{3}$, which means random distribution. This too-small domain size, which is less

than a typical domain wall width of a normal ferromagnet, strongly suggests that the ferromagnetic multidomain regime is not adequate and that the ferromagnetic long-range order disappears, which is in contrast to the case of the Au-Fe sample. It should be noted that the same behavior in the RSG of $\text{Rb}_2\text{Mn}_{1-x}\text{Cr}_x\text{Cl}_4$.²⁴

As described above, by estimating a domain size, we semiquantitatively showed that the magnetic state of the RSG phase on a mesoscopic scale is quite different for $\text{Fe}_{0.7}\text{Al}_{0.3}$ and $\text{Au}_{0.81}\text{Fe}_{0.19}$ alloys, in contrast to their similarity in low-field magnetization. Such a difference, however, may be understood by paying attention to the difference in the magnetic phase diagrams of two alloys, as well as the location of each sample in its phase diagram. In Fig. 9 we present a schematic drawing of the magnetic phase diagram of $\text{Fe}_x\text{Al}_{1-x}$ and $\text{Au}_{1-x}\text{Fe}_x$. Assuming the existence of a vertical line dividing the spin-glass phase into a pure spin-glass phase (denoted by SG in the figure) and a mixed phase of ferromagnetic and pure spin glasses (denoted by M in the figure), as predicted in the GT model, we can regard the RSG state of the $\text{Au}_{0.81}\text{Fe}_{0.19}$ sample as a mixed phase and that of the $\text{Fe}_{0.7}\text{Al}_{0.3}$ sample as a pure spin-glass phase. Because of the unusual shape of the phase boundary between the ferromagnetic and paramagnetic phases in the $\text{Fe}_x\text{Al}_{1-x}$ phase diagram, the $\text{Fe}_{0.7}\text{Al}_{0.3}$ sample exhibits a so-called re-entrant transition, through ferromagnetic, into pure spin glass, although it locates in the pure spin-glass side of the spin-glass phase.

Finally, we comment on the thermal evolution of P_0 . As given in Eq. (5), P_0 represents how the local magneti-

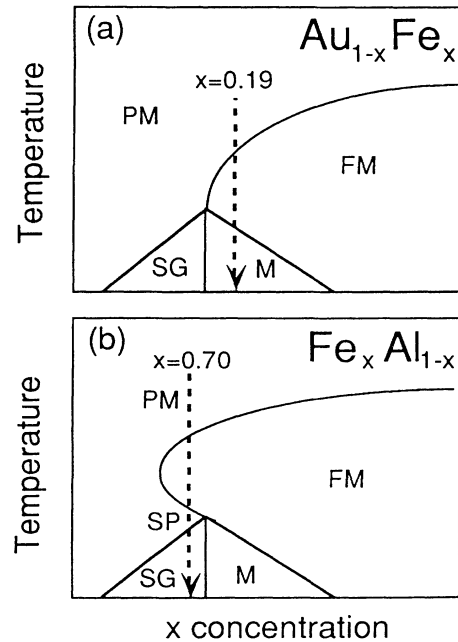


FIG. 9. Schematic drawings of the magnetic phase diagram for (a) $\text{Au}_{1-x}\text{Fe}_x$ and (b) $\text{Fe}_x\text{Al}_{1-x}$, where the location of each sample studied in the present experiments is shown by a dashed line. The symbols PM, FM, SP, SG, and M denote paramagnetic, ferromagnetic, superparamagnetic, pure spin-glass, and mixed phases, respectively.

zation of domains or clusters is aligned along the external field. When the sample enters into the ferromagnetic phase from the paramagnetic phase, the formation of domains reduces the average neutron polarization P_0 from unity. This behavior is clearly seen in the temperature dependence of P_0 on the Au-Fe sample near T_c . In the Fe-Al case, a near-zero value of P_0 in the ferromagnetic phase is unusual. By definition of P_0 given in Eq. (5), P_0 should take a value between 1 and $\frac{1}{3}$ for completely aligned and randomly orientated domain configuration, respectively. For the Au-Fe sample, this seems to be satisfied, as seen in Fig. 6(f). A near-zero value of P_0 means that most domains orientate perpendicular to the external magnetic field. At this moment we do not know why P_0 takes a near-zero value in the ferromagnetic phase, although a minor disturbance of the guide field due to the stray field from the sample itself might be a partial explanation. However, the different behavior of P_0 at temperatures below the ferromagnetic phase for both the Au-Fe and Fe-Al sample can be qualitatively understood as follows. In the Fe-Al case, as the spin-glass region gradually increases or the size of the ferromagnetic clusters is reduced below T_c^{inv} , the external magnetic field H_{ex} can align the local magnetization of the ferromagnetic clusters more effectively toward the field direction. Thus P_0 of the Fe-Al sample in the RSG phase increases below T_c^{inv} , as seen in Fig. 6(b). In contrast, in the Au-Fe case, as was explained above, ferromagnetic long-range order remains down to the lowest temperature; thus P_0 for the Au-Fe sample in the RSG phase is almost the same as P_0 for the ferromagnetic phase of the Au-Fe sample, as seen in Fig. 6(f).

To conclude, we have demonstrated the uniqueness of depolarization experiments to study the mesoscopically inhomogeneous internal magnetic field in magnetic ma-

terials. It has been shown that the RSG states as well as the magnetic state before entering the RSG state are quite different for Au-Fe and Fe-Al systems on a mesoscopic scale, although the low-field magnetization of both systems shows a similar rapid drop below T_g , except that the $\text{Fe}_{0.7}\text{Al}_{0.3}$ system has a magnetic state which looks like a superparamagnetic state between the ferromagnetic and RSG phases. The most probable process of the RSG transition in the Fe-Al sample is a decomposition of the continuously covered ferromagnetic network to many ferromagnetic clusters with a smaller size. On the other hand, the present depolarization experiments revealed the existence of a ferromagnetic multidomain state in the RSG phase of the Au-Fe sample. Such a multidomain state, as seen in the demagnetized state of a normal ferromagnet, strongly suggests that ferromagnetic long-range order remains in the RSG phase; in other words, ferromagnetic long-range order is coexistent with SG order in the RSG phase, which is consistent with the phase diagram predicted by the GT model.⁸ Finally, our inhomogeneous cluster picture on a mesoscopic scale for the Fe-Al sample might be related to a microscopic random-field picture.¹⁰

ACKNOWLEDGMENTS

The authors would like to thank Professor H. Sasaki, Professor N. Watanabe, and the late Professor Y. Ishikawa, for their encouragement to develop this depolarization method at KEK. We appreciate useful discussions with P. Boni, I. Mirebeau, K. Katsumata, S. M. Shapiro, Y. J. Uemura, and H. Aruga. One of us (S.M.) would like to thank Dr. Draaisma for critically reading this manuscript. The authors also would like to express their thanks to H. Fujimoto, S. Itoh, T. Watanabe, M. Onodera, and M. Suzuki for their assistance during the course of the experiments at Tohoku University.

*Present address: Physics Department, Science University of Tokyo, 1-3 Kagurazaka, Shinjyuku-ku, Tokyo 162, Japan.

¹K. Binder and A. P. Young, *Rev. Mod. Phys.* **58**, 801 (1986).

²H. Yoshizawa, S. Mitsuda, H. Aruga, and A. Itoh, *Phys. Rev. Lett.* **59**, 2636 (1987).

³M. Th. Rekveldt, *Z. Phys.* **256**, 391 (1973).

⁴I. Mirebeau, G. Jehanno, I. A. Campbell, F. Hippert, B. Hennion, and M. Hennion, *J. Magn. Magn. Mater.* **54-57**, 99 (1986).

⁵O. Halpern and T. Holstein, *Phys. Rev.* **59**, 960 (1941).

⁶S. Mitsuda and Y. Endoh (unpublished).

⁷Y. Ishikawa, Y. Endoh, and K. Inoue, in *Neutron Scattering in the Nineties*, Conference at Julich, Jan. 1985 (IAEA, 1985), p. 285.

⁸M. Gabay and G. Toulouse, *Phys. Rev. Lett.* **47**, 201 (1981).

⁹I. A. Campbell, S. Senoussi, F. Varret, J. Teillet, and A. Hamzic, *Phys. Rev. Lett.* **48**, 1490 (1982).

¹⁰G. Aeppli, S. M. Shapiro, R. J. Birgeneau, and H. S. Chen, *Phys. Rev. B* **28**, 5160 (1983); **29**, 2589 (1984).

¹¹K. Motoya, S. M. Shapiro, and Y. Muraoka, *Phys. Rev. B* **28**, 6183 (1983).

¹²S. Mitsuda, H. Yoshizawa, and Y. Endoh (unpublished).

¹³S. Mitsuda and Y. Endoh, *Phys. Soc. Jpn.* **54**, 1570 (1985).

¹⁴F. Mezei, in *Imaging Processes and Coherence in Physics*, edit-

ed by M. Schlenker, M. Fink, J. P. Goedgebuer, C. Malgrange, J. Ch. Viénot, and R. J. Wada (Springer-Verlag, Heidelberg, 1980), p. 282.

¹⁵I. Mirebeau, S. Itoh, S. Mitsuda, T. Watanabe, Y. Endoh, M. Hennion, and R. Papoular, *Phys. Rev. B* **41**, 11 405 (1990).

¹⁶S. Mitsuda, H. Yoshizawa, S. Itoh, T. Watanabe, Y. Endoh, and I. Mirebeau, *Phys. Soc. Jpn.* **60**, 1721 (1991).

¹⁷The constant c is 4.63×10^{-2} if Oe, cm, and Å units are used for B , L , and λ , respectively.

¹⁸R. D. Shull, H. Okamoto, and P. A. Beck, *Solid State Commun.* **20**, 863 (1978).

¹⁹B. R. Coles, B. V. B. Sarkissian, and R. H. Taylor, *Philos. Mag. B* **37**, 489 (1978).

²⁰Y. Endoh, Y. Sasaki, H. Ono, S. Mitsuda, and S. Ikeda, *Physica* **120B**, 45 (1983).

²¹Y. Endoh, S. Ikeda, S. Mitsuda, and H. Fujimoto, *Nucl. Instrum. Methods A* **240**, 115 (1985).

²²S. Senoussi, S. Hadjoudj, and R. Fourmeaux, *Phys. Rev. Lett.* **61**, 1013 (1988).

²³I. Mirebeau, S. Itoh, S. Mitsuda, T. Watanabe, Y. Endoh, M. Hennion, and R. Calmettes, *J. Appl. Phys.* **67**, 5232 (1990).

²⁴K. Katsumata, M. Tanimoto, S. Mitsuda, and Y. Endoh, *Phys. Soc. Jpn.* **53**, 3315 (1984).

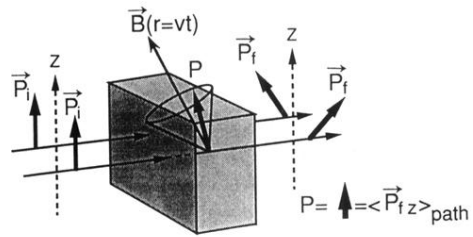


FIG. 1. Schematic drawing of the Larmor precession of a neutron-polarization vector \mathbf{P} of a subbeam in a magnetic material: \mathbf{P}_i is the incident polarization vector which is fully polarized along the z direction. \mathbf{P}_f is the final polarization vector of a subbeam which points out in some direction, reflecting the Larmor precession around the internal field $\mathbf{B}(r)$ along the neutron subbeam. P is the polarization of the whole transmitted beam used in the experiment, which is defined by the average of the z component of the vector \mathbf{P}_f over all subbeams. Note that the norm of the polarization vector of the subbeams is kept to unity, namely, $|\mathbf{P}_i| = |\mathbf{P}| = |\mathbf{P}_f| = 1$.

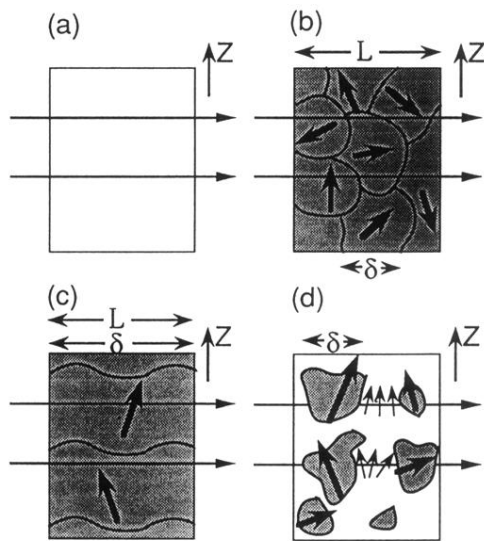


FIG. 2. Schematic drawing of typical magnetic inhomogeneities: (a) spin-glass case, (b) ferromagnetic multidomain case, (c) ferromagnetic monodomain case, and (d) superparamagneticlike case. The sample is magnetized along the z axis. White and hatched regions correspond to pure spin-glass and ferromagnetically aligned regions, respectively. The arrow represents the direction of the local magnetization of each domain or cluster. The small arrows in the white region of model case (d) represent the stray field from the clusters.

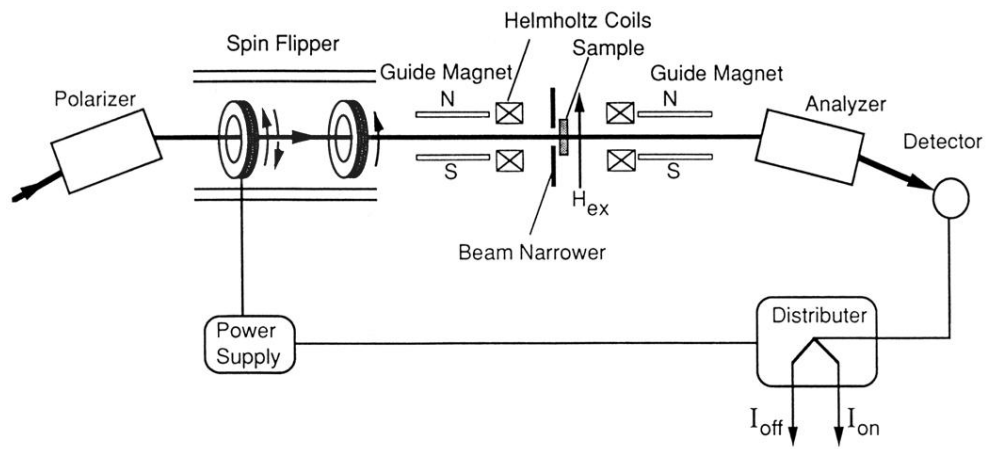


FIG. 4. Schematic drawing of experimental setup to measure neutron depolarization.